PAPER

Check for updates

Kaolin-derived sodalite nanocatalyst for sustainable biodiesel production

Abdul Hamid, ID *[a] Yusuf Widayanto,[a] Zeni Rahmawati, ID *[b] Misbakhul Fatah,[a] Tri Esti Purbaningtias,[c] Tri Wahyuni[d] and Ike Dayi Febriana[a]

Sodalite was successfully synthesized from natural kaolin as a nanocatalyst for biodiesel production using *Reutealis trisperma* oil (RTO). The synthesis of sodalite was conducted at crystallization temperatures of 80, 100 and 120 °C. The pure sodalite phase was formed at a crystallization temperature of 100 °C, as confirmed by characterization using FTIR spectroscopy and XRD. The sodalite catalyst demonstrated outstanding performance in the catalytic conversion of RTO into biodiesel. The optimum biodiesel yield and conversion achieved under a molar ratio of oil to methanol of 1 : 30 using the S-100 catalyst were 94.14% and 81.79%, respectively. Unlike conventional CaO or NaOH catalysts, kaolin-derived sodalite provides a low-cost, reusable alternative with enhanced efficiency. This study demonstrates the potential of sodalite as a sustainable nanocatalyst, supporting clean energy development and contributing to the United Nations Sustainable Development Goals, particularly SDG 7 (Affordable and Clean Energy) and SDG 13 (Climate Action).

Introduction

The increasing demand for energy, especially fuel oil, will inevitably arise owing to the growing number of vehicles as well as new industries.[1] The declining availability of fossil fuel sources has been a global concern over the past few years. One of the ways to resolve this problem is to develop renewable energy sources that are reproducible and sustainable.[2,3] Among various alternative energy sources to fossil fuels, biodiesel has played an important role due to its advantages, such as flexibility in raw materials; low emission levels of CO, NO_x, and SO_x; biodegradability; non-toxicity; and a high cetane number.[4,5] Biodiesel is often produced from natural resources that are also consumed by humans; hence, developing non-edible raw materials is a main priority. The *Reutealis trisperma* plant can be developed as a potential biodiesel feedstock. Furthermore, *Reutealis trisperma* seeds contain a high amount of vegetable oil, approximately 50–56%.[6] This plant is abundantly available and widely cultivated in West Java, Indonesia, making it a promising local non-edible feedstock for biodiesel production.

Holilah *et al.* reported the production of biodiesel derived from RTO using a homogeneous NaOH catalyst.[7] The feasibility of utilizing non-edible *Reutealis trisperma* oil as a novel carbon

[a]Department of Mechanical and Industrial Engineering, Politeknik Negeri Madura, Sampang, Indonesia. E-mail: ahamchimie@poltera.ac.id

[b]Chemistry Department, Faculty of Science and Data Analytics, Institut Teknologi Sepuluh Nopember, Surabaya, Indonesia. E-mail: zeni.rahmawati@its.ac.id

[c]Chemistry Department, Faculty of Mathematics and Natural Sciences, Universitas Islam Indonesia, Yogyakarta, Indonesia

[d]Dharma Wanita 1 Senior High School, Pare, Kediri, Indonesia

feedstock for biodiesel production was evaluated. The kernels contained 50–52 wt% oil when extracted using the hot pressing method. Crude oil was directly converted into biodiesel without prior purification. Methanol concentration, reaction temperature, and catalyst loading were identified as critical parameters for achieving a high biodiesel yield. Under the optimized conditions, a maximum yield of 95.15% was obtained at 65 °C. Rahmawati *et al.* presented a study focusing on RTO biodiesel derived through transesterification using a CaO–ZnO catalyst.[8] Parameters, including the methanol-to-oil ratio, reaction time, and Ca/Zn composition, were optimized using the Taguchi method. Statistical analysis indicated similar contribution percentages for the reaction time and the Ca/Zn composition parameter, each around 35%, while the methanol-to-oil ratio showed a contribution of 26.6%. The optimal conditions predicted using the S/N ratio were a Ca/Zn composition of 1, reaction time of two hours, and methanol-to-oil ratio of 30, which resulted in an optimum yield of 98%. The study also suggested that RTO could potentially be used as crude oil for biodiesel production.

The efficiency of biodiesel production largely depends on the catalyst employed in the transesterification process. Based on the previous explanation, homogeneous catalysts, such as NaOH, are widely used due to their high reactivity, but they suffer from drawbacks such as soap formation, catalyst recovery challenges, and wastewater generation.[9,10] Heterogeneous catalysts, like CaO, offer better separation but are prone to leaching, which reduces their stability and reusability.[11] Mixed oxide systems, such as CaO–ZnO, can improve activity but still face limitations in terms of long-term durability and synthesis

complexity.[12] Zeolite-based catalysts have also been applied due to their well-defined pore structure and thermal stability. However, their synthesis often relies on expensive commercial precursors, such as sodium aluminate or colloidal silica, restricting their large-scale application.[13] To address these limitations, sodalite-type zeolite has emerged as a promising heterogeneous catalyst due to its strong basicity, thermal stability, and cage-like structure, which enhance the catalytic activity. Importantly, sodalite can be synthesized from natural kaolin, which is an abundant and inexpensive clay mineral that is rich in silica and alumina. Kaolin is widely distributed in Indonesia, particularly in the Bangka Belitung Islands.[14] The abundant availability of kaolin in Bangka Belitung provides a strategic opportunity to develop value-added applications beyond conventional uses. The utilization of kaolin as a precursor reduces synthesis costs and promotes the use of local, sustainable resources for catalyst development.[15] Furthermore, converting kaolin into advanced catalytic materials for biodiesel production exemplifies a circular-economy approach in which natural resources are upgraded into high-performance, environmentally friendly technologies. This approach represents a significant step toward more sustainable and affordable biodiesel production. Table 1 summarizes the various catalysts employed in biodiesel production from *Reutealis trisperma* oil (RTO), along with their respective advantages and disadvantages. This work aims to synthesize sodalite from natural kaolin at different crystallization temperatures, characterize its physicochemical properties, evaluate its catalytic activity in biodiesel production from non-edible *Reutealis trisperma* oil, and measure its effect on diesel engine emissions.

Experimental

Materials

The materials employed in this study were *Reutealis trisperma* seeds retrieved from local sellers in West Java, Indonesia; natural kaolin containing approximately 46% Si and 22% Al, sourced from Bangka Belitung, Indonesia, sulfuric acid (H_2SO_4, 98%, Smart Lab); methanol for the analysis (CH_3OH, 99.8%, Merck); sodium hydroxide (NaOH, ≥98%, Merck); sodium aluminate ($NaAlO_2$, ≥98%, Sigma-Aldrich); isopropanol (C_3H_7OH, 99.8%, Merck); phenolphthalein indicator (Merck) and demineralized water. The main instruments used for catalyst characterization included FTIR, XRD, SEM-EDX, nitrogen adsorption–desorption, and GC-MS.

Synthesis of sodalite from natural kaolin

The synthesis process began by dissolving sodium hydroxide pellets (8.94 g) in demineralized water (105.48 g) in a polypropylene bottle. Kaolin (12 g) was then added and stirred at 600 rpm for 15 minutes until a homogeneous mixture was obtained, followed by the addition of sodium aluminate (3.6 g). The mixture was aged at room temperature for 24 h and subsequently crystallized at 80, 100, and 120 °C for 24 h in an oven. After cooling with running water, the solid product was filtered, washed with demineralized water until the pH reached 8–9, and dried at 100 °C for 24 h. The synthesized samples were designated as S-80, S-100, and S-120. Fig. 1 illustrates the sodalite synthesis process, and the synthesis conditions are presented in Table 2.

Table 1 Summary comparing various catalysts employed in the biodiesel production from *Reutealis trisperma* oil (RTO)

| Catalyst	Reaction conditions	Biodiesel yield (%)	Advantages	Disadvantages	References
Sodium hydroxide (NaOH)	1 hour, 70 °C, 1 wt%, 1 : 6	96.38	High yield, fast reaction and widely available	Not reusable, sensitive to free fatty acids (FFA), leading to soap formation, produces wastewater (environmental issue)	Supriyadi *et al.*[16]
ZnO from limestone	3 hours, 65 °C, 5 wt%, 1 : 15	52.34	Heterogeneous and reusable, cheap and abundant natural source, more eco-friendly than homogeneous	Long reaction and high methanol ratio, limited activity without modification	Shalihah *et al.*[17]
Potassium hydroxide (KOH)	1.5 hours, 60 °C, 0.5 wt%, 1 : 60	95.29	High yield and fast reaction	Not reusable, sensitive to free fatty acids (FFA), leading to soap formation, more expensive than NaOH, produces wastewater (environmental issue)	Riayatsyah *et al.*[18]
CaO–ZnO	1 hour, 60 °C, 3 wt%, 1 : 30	94.7	High yield, synergistic effect improves activity	Complex preparation and risk of metal leaching	Rahmawati *et al.*[19]
KOH impregnated CaO	1 hour, 60 °C, 7 wt%, 1 : 12	97.95	High yield, short reaction	Preparation is more complex, risk of K leaching	Kusmiyati *et al.*[20]
CaO from limestone	2 hours, 60 °C, 1 wt%, 1 : 1	56.13	Cheap, sustainable (natural resource), reusable and eco-friendly	Low yield, requires high calcination temperature	Suprapto *et al.*[21]
Sodalite from natural kaolin	2 hours, 65 °C, 4 wt%, 1 : 30	94.14	High yield, sustainable (kaolin abundant in Indonesia), high surface area, reusable, better stability than simple oxides	Requires synthesis (hydrothermal/alkaline), activity may drop after reuse	This work
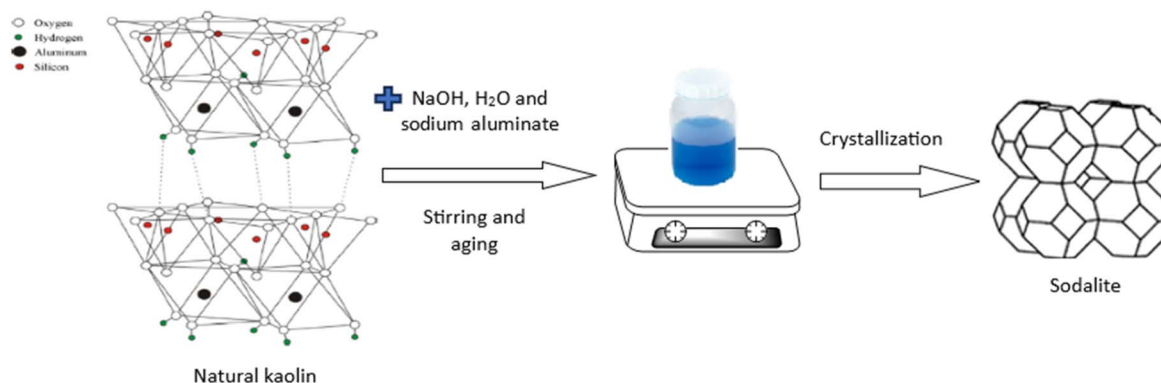
Fig. 1 Stages of the sodalite synthesis process from natural kaolin.

Table 2 Sodalite synthesis conditions

Sample	Si/Al molar ratio	NaOH/kaolin molar ratio	Crystallization temperature (°C)	Crystallization time (h)
S-80	2	1.5	80	24
S-100	2	1.5	100	24
S-120	2	1.5	120	24

A stirring speed of 600 rpm was selected to ensure homogeneous dispersion of the precursors without causing excessive turbulence, which might disrupt crystal nucleation. Crystallization temperatures of 80, 100, and 120 °C were chosen to evaluate the influence of thermal energy on sodalite phase formation. Lower temperatures favor slow nucleation, intermediate temperatures provide balanced crystal growth, and higher temperatures accelerate crystallization but may lead to secondary phase formation. According to previous studies, most zeolite crystallizations occur within the temperature range of 80–150 °C over a 24 h period. Therefore, this study aims to investigate the effect of crystallization temperature on sodalite phase formation.

Characterization

Catalyst characterization involved XRD, FTIR, nitrogen adsorption–desorption, and SEM-EDX analyses. XRD measurements were carried out using CuKα radiation on an XRD diffractometer (Bruker D2 Phaser) at 2θ angles ranging from 5° to 60° with $\lambda = 1.54056$ Å to determine the crystalline phases and degree of crystallinity. Relative crystallinity (%) was calculated based on the ratio of the diffraction peak intensity of the sample to that of the reference sample with the highest intensity, as shown in the following equation:

$$\text{Relative crystallinity} = \frac{\text{Total intensity value of sample}}{\text{Total intensity value of reference}} \times 100\%.$$

FTIR characterization was performed using a Nicolet Avatar 360 IR spectrometer employing KBr pellets and a wavenumber range of 500–1400 cm^{-1} to identify the functional groups present in the catalysts. In addition, the solids were characterized using a SEM–EDX instrument (Hitachi FlexSEM 100) to examine the morphology and elemental composition of the catalysts. The catalysts were coated with Pd/Au for 15 s under a pressure of 6×10^{-2} mbar using the ion-sputtering coating method before being mounted on a carbon tape base. Meanwhile, the pore volume, surface area, and pore size of all samples were determined using nitrogen adsorption–desorption measurements with a Quantachrome NovaTouch LX4 instrument. Prior to analysis, the samples were degassed at 300 °C. The surface areas and pore size distributions were analyzed using the Brunauer–Emmett–Teller (BET) and Barrett–Joyner–Halenda (BJH) methods, respectively.

Biodiesel production from *Reutealis trisperma* oil (RTO)

The extraction of crude oil from *Reutealis trisperma* involved pressing and straining processes to remove impurities. Subsequently, H_3PO_4 (0.5% w/w of the crude oil) was added to the filtered crude oil at 80 °C and stirred at 400 rpm for 15 minutes for the degumming process. The degummed oil was mixed with methanol at a 9 : 1 molar ratio, followed by the addition of a 2% (w/w) H_2SO_4 catalyst at 65 °C and stirring at 900 rpm for 2 h for the esterification process. The esterified product was subsequently subjected to the transesterification process. In this process, methanol was first reacted with a 1% (w/w) S-80 catalyst under continuous stirring, followed by the addition of pre-esterified oil. The molar ratios of methanol to oil used in the transesterification process were 20 : 1 and 30 : 1. Transesterification process was carried out at 65 °C with stirring at 900 rpm for 2 h. The resulting mixture was allowed to settle into two layers. The biodiesel layer was then analyzed using GC-MS.

The same procedure was repeated using the S-100 and S-120 catalysts.

Biodiesel product analysis

The free fatty acid (FFA) content in RTO and the esterified oil was analyzed using an acid–base titration method based on AOCS Ca 5a–50.[22] Initially, 0.1 g of the oil sample was placed in an Erlenmeyer flask, and 3 mL of isopropanol was added and heated to 40 °C until completely dissolved. Subsequently, three drops of phenolphthalein indicator were added and titrated with 0.01 N NaOH solution until a persistent pink color appeared. The FFA content was calculated using the following equation:[23]

$$\%FFA = \frac{V \times N \times Mr}{m \times 10},$$

where V is the volume of NaOH (mL), N is the normality of NaOH, Mr is the molecular weight of linoleic acid (g mol^{-1}), and m is the mass of the sample (g).

The conversion and biodiesel yield were analyzed using gas chromatography-mass spectrometry (GC-MS, Shimadzu QP 2010 SE) equipped with an RTX capillary column (length 30.0 m, internal diameter 0.25 mm, and film thickness 0.25 μm) at a flow rate of 0.46 mL min^{-1}. The injector temperature was set to 250 °C, while the oven temperature was initially held at 80 °C and then increased to 300 °C at a heating rate of 10 °C min^{-1}.

Methyl heptadecanoate was used as the internal standard in this study. The conversion and methyl ester yields were calculated using the following equations:[24,25]

$$\text{Oil conversion} = \frac{\text{Weight of initial oil} - \text{weight of residual}}{\text{Weight of initial oil}} \\ \times 100\%,$$

$$\text{Metil ester yield} = \left(\frac{\sum A_{ME}}{A_{is}}\right)\left(\frac{C_{is} \times V_{is}}{m_s}\right) \times 100\%,$$

where $\sum A_{ME}$ denotes the total peak area of methyl ester (C8 : 0 to C24 : 1), A_{is} is the internal standard peak area, C_{is} is the internal standard concentration (g mL^{-1}), V_{is} is the internal standard volume (ml) and m_s is the sample mass (mg). The produced biodiesel was also analyzed for exhaust gas emissions, including NO, NO$_x$, and CO, using a gas analyzer with various fuel blend compositions.

Results and discussion

The XRD characterization results of kaolin and the synthesized catalysts are presented in Fig. 2. Diffraction peaks corresponding to the kaolinite phase appeared at 2θ values of approximately 12.31°, 20.38°, 24.78°, 35.86°, and 45.69°.[26,27] In addition, the diffractogram of the kaolin sample was characterized by a broad peak appearing at $2\theta = 35°–40°$.[28] The X-ray diffraction pattern of S-80 showed that the kaolinite phase was still present, with diffraction peaks observed at approximately $2\theta = 12.36°$, 19.91°, 24.91°, and 38.94°. The relatively low crystallization temperature during synthesis did not promote the transformation from the kaolinite phase to sodalite. This occurred because kaolin did not completely dissolve at relatively low temperatures; hence, the Si–O–Al bonds, which form the zeolite framework, could not be fully developed through polymerization and condensation reactions during crystallization.[29] The sodalite phase fully appeared when the crystallization temperature was increased to 100 °C, whereas the kaolinite phase diminished, indicating the formation of sodalite. Distinct diffraction peaks were observed in the S-100 and S-120 samples at approximately $2\theta = 13.94°$, 24.26°, 31.82°, 34.61°, and 42.68°. These diffraction peaks were consistent with previous studies by Cui *et al.*[30] and Arepalli *et al.*,[31] in which sodalite diffraction peaks appeared at $2\theta = 14.08°$, 24.42°, 31.64°, 34.72°, and 42.84°, corresponding to the crystallographic planes (110), (211), (310), (222), and (330), respectively. Based on the
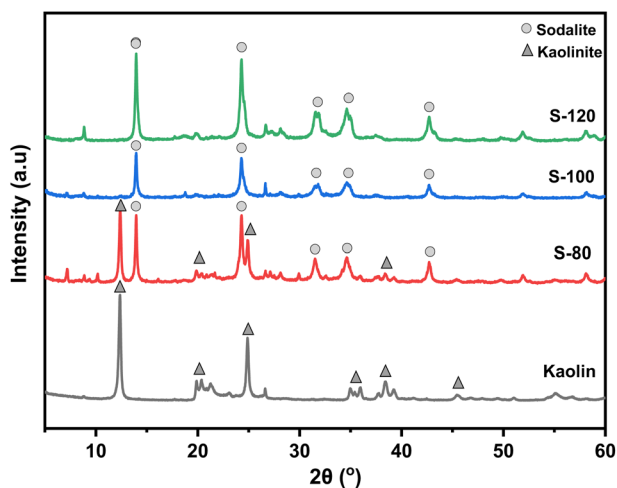

Fig. 2 Diffractogram patterns of the kaolin samples: S-80, S-100 and S-120.

Table 3 Summary of the diffraction peaks (2θ values), corresponding phases, and products formed in kaolin samples: S-80, S-100, and S-120

| Sample | Phase (2θ) | | Product |
	Kaolinite	Sodalite	
Kaolin	12.31°, 20.38°, 24.78°, 35°–40°, 35.86° and 45.69°	—	Kaolinite
S-80	12.36°, 19.91°, 24.91°, and 38.94°	13.94°, 24.26°, 31.82°, 34.61°, and 42.68°	Kaolinite and sodalite
S-100	—	13.94°, 24.26°, 31.82°, 34.61°, and 42.68°	Pure sodalite
S-120	—	13.94°, 24.26°, 31.82°, 34.61°, and 42.68°	Pure sodalite

diffractogram shown in Fig. 2, the formation of the sodalite phase was stable when synthesized at a crystallization temperature of 100 °C. The total peak intensity in the sodalite diffractogram correlated with the degree of crystallinity. The highest degree of crystallinity for sodalite was obtained in the S-120 sample, followed by the S-80 and S-100 samples (Table 5). The relative crystallinity of sodalite was observed to decrease as the synthesis temperature increased from 80 °C to 100 °C, followed by a subsequent increase at 120 °C. This behavior can be attributed to the dynamic balance between the dissolution, nucleation, and crystal growth processes during hydrothermal synthesis. At 80 °C, the system favors the formation of numerous sodalite nuclei as kaolinite partially dissolves, resulting in relatively high crystallinity. Crystallinity appears relatively high because many nuclei form simultaneously though the crystals are still small. When the temperature increases to 100 °C, the rate of dissolution of aluminosilicate species exceeds the rate of crystal growth, leading to the formation of amorphous intermediates and a temporary reduction in sodalite crystallinity. However, further increasing the temperature to 120 °C enhances the mobility of the Al and Si species, promoting recrystallization and the development of well-ordered sodalite crystals. Consequently, crystallinity increases again as the system approaches a more thermodynamically stable phase.

Table 3 summarizes the diffraction peaks (2θ values), corresponding phases, and products formed in kaolin, S-80, S-100, and S-120 samples. When the crystallization temperature increased to 100 °C and 120 °C (samples S-100 and S-120), only sodalite peaks remained, accompanied by the complete disappearance of kaolinite signals. This confirms that higher crystallization temperatures promote the total conversion of the kaolinite structure into sodalite. The absence of kaolinite reflections indicates that the layered structure of kaolin has been entirely reorganized into the sodalite framework. These findings emphasize the critical role of temperature in governing phase transformation: lower temperatures allow the coexistence of mixed phases, while higher temperatures favor the complete crystallization and phase purity of sodalite, which is desirable for applications requiring uniform zeolitic properties.

The transformation of the kaolinite phase into sodalite, as observed from the FTIR spectra, is shown in Fig. 3. The absorption bands of kaolin were observed at 1116, 1029, 913, 791, 755, 694, and 540 cm^{-1}. The Si–O stretching vibrations appeared at peaks around 1107 and 1029 cm^{-1},[32] while the Al–OH stretching vibrations were detected at approximately 913 cm^{-1}, indicating the deformation of hydroxyl (OH) groups within the inner and surface regions of kaolinite.[33,34] The skeletal vibration of Al–O in Al[O(OH)]$_6$ was observed at around 541 cm^{-1}.[35] The absorption bands at 755 and 795 cm^{-1} correspond to the symmetric stretching of Si–O–Al,[34] while the band at 694 cm^{-1} is attributed to Al–O–H vibrations.[36] In addition, the absorption band at 540 cm^{-1} corresponds to Al–O deformation. The S-80 sample displayed the kaolinite phase, as indicated by slightly flattened peaks at 1116, 1029, and 913 cm^{-1}, along with a sharp peak at 540 cm^{-1}. This observation is consistent with the XRD results, which confirmed that the kaolinite phase was
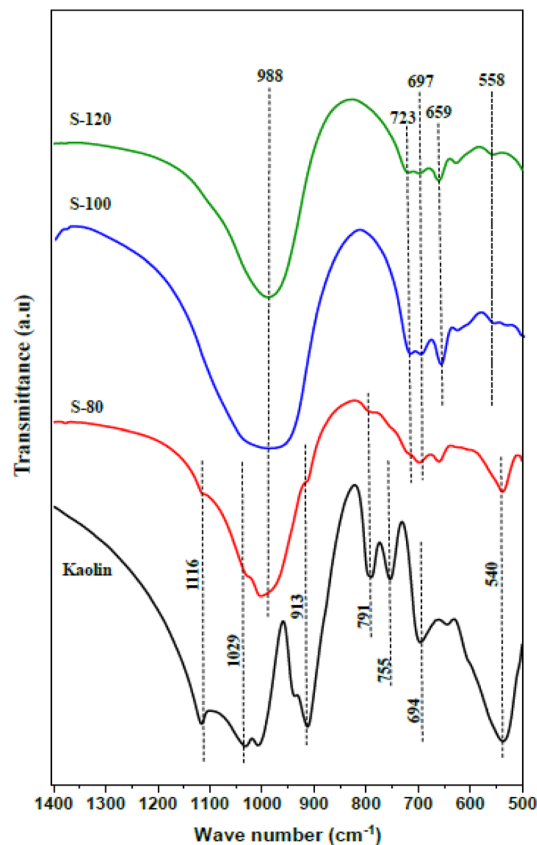

Fig. 3 IR spectra of the kaolin samples: S-80, S-100 and S-120.

formed at a crystallization temperature of 80 °C. Some unreacted kaolinite remained in the synthesized product at this temperature, hindering the complete formation of sodalite, as verified by XRD analysis. The characteristic absorption band of sodalite, shown in Fig. 3, includes a peak at 988 cm^{-1}, corresponding to the asymmetric stretching vibration of T–O–T (where T = Si or Al).[36] Additionally, peaks at 723 cm^{-1} and 659 cm^{-1} indicate symmetric stretching vibrations of T–O–T.[37] The band at 697 cm^{-1} is associated with Al–O–H vibrations, while the band at 558 cm^{-1} corresponds to the deformation of Al–O.

The results summarized in Table 4 indicate that, at higher crystallization temperatures (S-100 and S-120), the disappearance of kaolinite-specific bands and the dominance of sodalite vibrations (988, 723, 659, 697, and 558 cm^{-1}) confirm a complete structural transformation. This progression demonstrates that higher temperatures provide sufficient energy for the full reorganization of layered kaolinite into a three-dimensional sodalite framework. These findings are significant, as they corroborate the complementary XRD evidence. At lower temperatures, incomplete transformation leaves residual kaolinite, while at higher temperatures, pure sodalite with well-defined framework vibrations is obtained. This structural evolution is crucial for catalytic applications, where the purity and crystallinity of sodalite strongly influence its performance.

Table 4 FTIR bands of kaolin samples: S-80, S-100, and S-120

Sample	Absorption bands (cm^{-1})	Vibration assignments
Kaolin	1116, 1029	Si–O stretching vibrations
	913	Al–OH stretching (inner/surface OH deformation)
	791, 755	Symmetric stretching of Si–O–Al
	694	Al–O–H transformation
	540	Skeletal vibration of Al–O in Al[O(OH)]$_6$
S-80	1116, 1029 (weak)	Si–O stretching vibrations (kaolinite residuals)
	988	Asymmetric stretching vibration of T–O–T (T = Si or Al) – sodalite
	913 (weak)	Al–OH stretching (kaolinite residuals)
	723, 659	Symmetric stretching vibration of T–O–T – sodalite
	697 (weak)	Al–O–H vibration – sodalite
	540	Skeletal vibration of Al–O (kaolinite phase)
S-100 and S-120	988	Asymmetric stretching vibration of T–O–T (T = Si or Al) – sodalite
	723, 659	Symmetric stretching vibration of T–O–T – sodalite
	697	Al–O–H vibration – sodalite
	558	Al–O deformation – sodalite

Table 5 Physicochemical characterization results of the catalyst samples

Samples	Phases	Relative crystallinity (%)	Elemental composition (% weight)			Si/Al (mole ratio)
			Si	Al	Na	
S-80	Kaolin and sodalite	82.69	22.03	21.44	18.52	0.99
S-100	Sodalite	63.16	23.56	22.02	19.20	1.03
S-120	Sodalite	100	24.59	22.36	19.03	1.06

The SEM–EDX analysis of the S-100 and S-120 samples revealed similar surface morphologies characterized by irregular spherical aggregates, as shown in Fig. 4. However, the S-80 sample exhibited a slightly oval-shaped morphology of kaolin, marked by a red circle. The remaining plate-like kaolin structures indicated the presence of unreacted kaolinite at low synthesis temperatures. The particle size distribution analysis, obtained from SEM images using ImageJ software, showed that sodalite particles were predominantly 10–20 nm in size, as shown in Fig. 5. In contrast, S-120 exhibited a slightly larger particle size distribution (∼20 nm) compared to the other samples. At low temperatures (80 °C), kaolin does not fully dissolve, resulting in the incomplete release of Si and Al into the synthesis gel and leaving some Al trapped within the kaolinite layers, which lowers the effective Si/Al ratio in the product. At higher temperatures (100–120 °C), kaolin dissolution becomes more complete. However, since Al–O bonds are stronger than Si–O bonds, aluminum dissolves more slowly than silicon. Consequently, increasing the crystallization temperature promotes greater incorporation of Si into the sodalite framework, slightly raising the Si/Al ratio.

The EDX results confirmed that the S-80, S-100, and S-120 samples contained the key elements of sodalite (Si, Al, Na, and O), as shown in Fig. 5 and Table 1. The S-80 sample exhibited lower Si and Al distributions compared to the S-100 and S-120 samples, indicating limited silica and alumina dissolution at lower temperatures. The Si/Al molar ratio increased slightly from 0.99 (S-80) to 1.03 (S-100) and 1.06 (S-120), reflecting greater silica incorporation into the sodalite

framework with rising crystallization temperatures. A balanced Si/Al ratio enhances basicity and facilitates triglyceride activation during transesterification. The optimal ratio in S-100 provided sufficient basic sites and structural stability, while S-120, despite a slightly higher ratio, showed reduced surface area and mesoporosity, limiting active site accessibility and slightly lowering biodiesel yield (93.44%). Thus, the superior catalytic performance of S-100 results from its favorable morphology and optimal Si/Al ratio.

The largest particle sizes among all sodalite samples were approximately 120–140 nm. During sodalite synthesis, silica and alumina polymerization occurred to form amorphous aluminosilicate particles, which were subsequently organized into a three-dimensional structure due to electrostatic interactions between the particles, forming a rigid gel network. At relatively low crystallization temperatures, the solubility of aluminosilicate species decreased, leading to mixed-phase formation with incomplete sodalite crystallization.[38]

The nitrogen adsorption–desorption isotherm of the sodalite samples is shown in Fig. 6. For the S-80 sample, nitrogen adsorption was relatively low at relative pressures (P/P_0) between 0 and 0.7. Meanwhile, a higher amount of nitrogen adsorption was observed at relative pressures (P/P_0) between 0.7 and 1. At a P/P_0 of approximately 0.7, the surface of the catalyst became covered by nitrogen molecules, resulting in the formation of a monolayer.[39] Subsequently, a significant increase in the volume of adsorbed nitrogen was observed, indicating the presence of a hysteresis loop, which is characteristic of
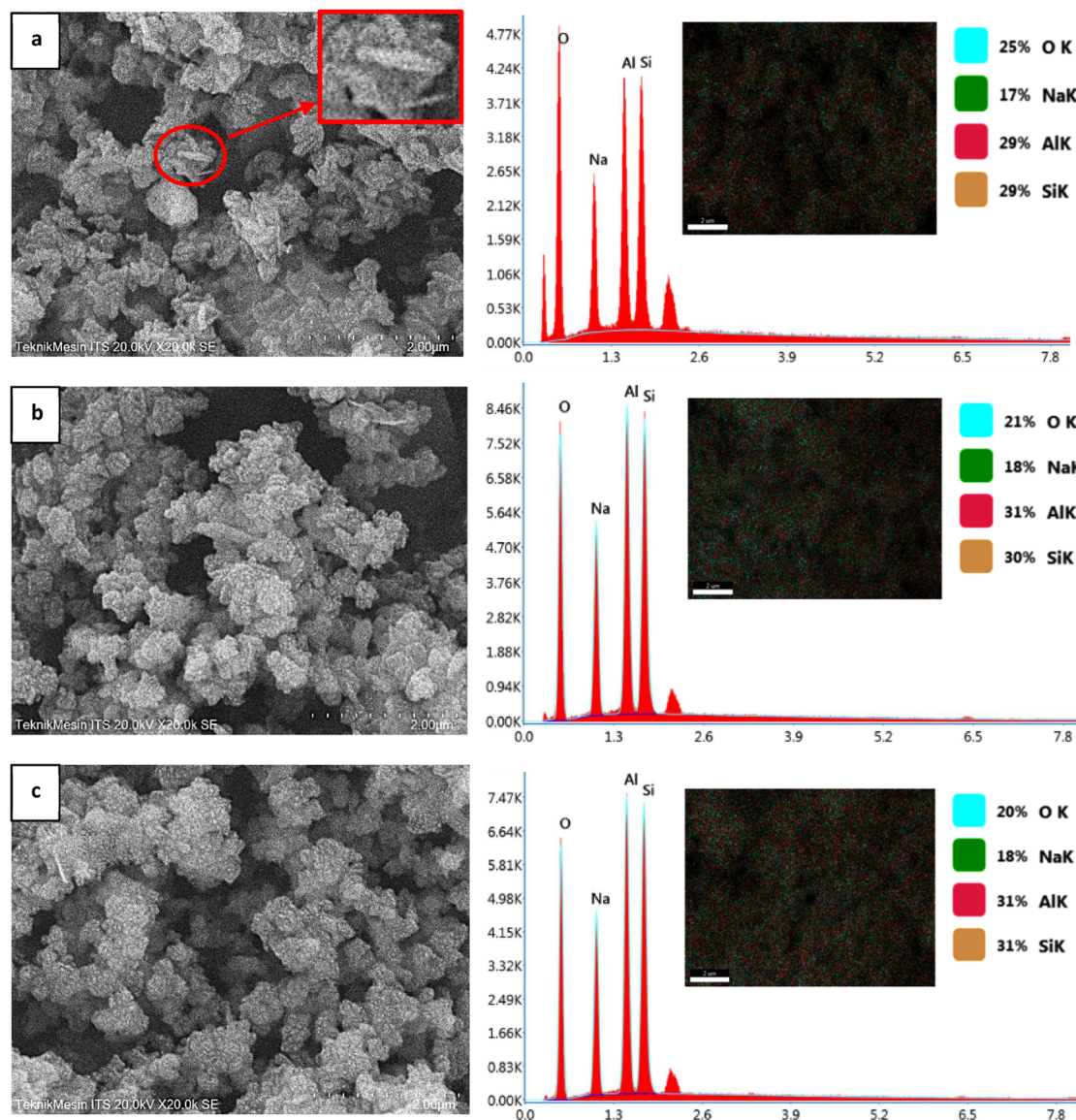
Fig. 4 SEM-EDX of the catalyst samples: S-80 (a), S-100 (b) and S-120 (c).

mesoporous materials. The hysteresis loops in S-100 and S-120 appeared larger than those in S-80.

The difference in the number of adsorbed and desorbed nitrogen molecules causes a hysteresis loop to occur. Based on

the isotherm pattern in Fig. 6, the sodalite samples exhibited a type IV isotherm profile, which represents the characteristics of a solid with a mesoporous structure. Type IV isotherms are characterized by several distinct stages. In the initial stage,
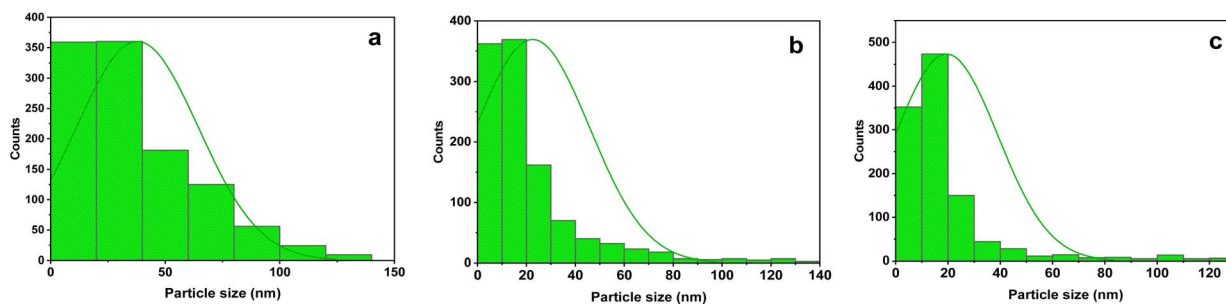
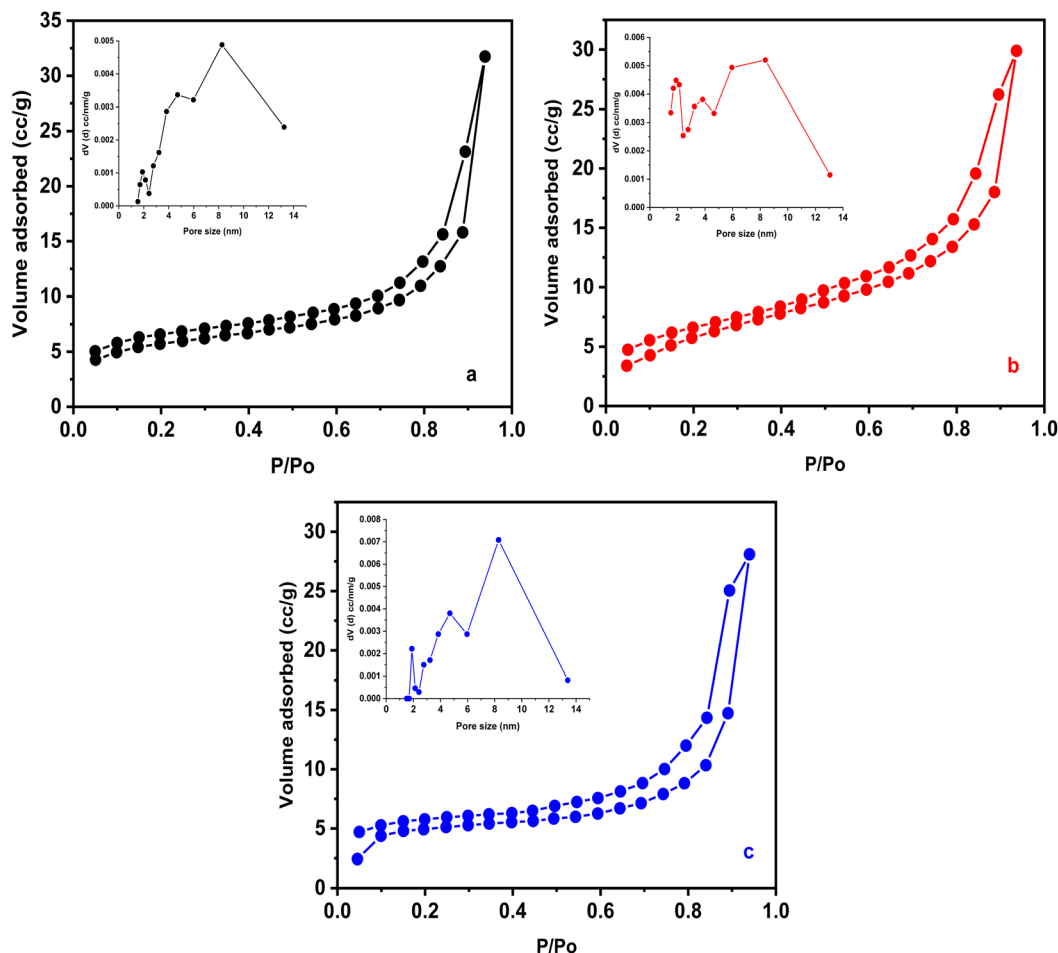**Fig. 5** Particle size distribution of the catalyst samples: S-80 (a), S-100 (b) and S-120 (c).

Fig. 6 N$_2$ adsorption–desorption isotherms and pore size distribution (insets) of S-80 (a), S-100 (b) and S-120 (c).

nitrogen molecules were gradually adsorbed onto the surface of the material as the relative pressure (P/P_0) increased to below 0.7. At this relative pressure, isothermal capillary condensation occurred, initiating the formation of multilayer adsorption.[39]

In the following stage, the pronounced increase in nitrogen adsorption at a relative pressure (P/P_0) of 0.7–0.95 indicates the filling of mesopores with nitrogen molecules, corresponding to multilayer adsorption on the pore walls. The surface area obtained from the N$_2$ adsorption–desorption analysis using the BET method is presented in Table 6. The largest surface area was observed for S-100 (Table 6). The surface area of synthesized sodalite samples (22.59 m^2 g^{-1}), followed by S-80 and S-120 (19.34 m^2 g^{-1} and 15.85 m^2 g^{-1}, respectively). The three samples exhibited mesoporous structures, with pore diameters

ranging from 2 to 14 nm, as shown in Fig. 6. The highest pore size intensity was observed for S-100 and S-120 at a diameter of around 8.29 nm. This observation is further supported by the higher mesopore surface areas of samples S-100 and S-120, which were 16.89 m^2 g^{-1} and 12.05 m^2 g^{-1}, respectively (Table 6). This indicates a reduction in the amorphous sodalite phase with increasing crystallization temperature, as observed when the temperature was increased from 100 to 120 °C. The total pore volume and micropore surface area of the catalyst samples also decreased as the crystallization temperature increased owing to the higher degree of crystallinity in the sodalite samples.

At low crystallization temperatures (around 80 °C), kaolinite remains largely undissolved in an alkaline solution, resulting in

Table 6 Textural properties of the synthesized sodalite samples

Samples	S_{BET} (m^2 g^{-1})	S_{micro} (m^2 g^{-1})	S_{meso} (m^2 g^{-1})	Pore size (nm)	Vol total (cm^3 nm^{-1} g^{-1})
S-80	19.34	7.49	11.85	8.26	0.049
S-100	22.59	5.7	16.89	8.29	0.046
S-120	15.85	3.81	12.04	8.29	0.044

only partial breakdown of the Si–O–Al framework. Because the dissolution of silica and alumina species is limited, the polymerization and condensation reactions required to form the zeolitic sodalite framework cannot proceed efficiently. As a result, kaolinite plate-like morphologies are still visible, and XRD patterns show residual kaolinite peaks, indicating that the transformation into sodalite has not yet occurred. This incomplete dissolution hinders the development of mesoporosity and limits the availability of active basic sites for catalysis. When the crystallization temperature is increased to 100 °C, the dissolution of alumina and silica becomes more effective, allowing reorganization into a sodalite framework characterized by the formation of β-cages. This balance results in pure sodalite with moderate crystallinity and the highest mesoporous surface area, enhancing catalytic accessibility. At 120 °C, however, higher thermal energy drives more extensive crystallization, producing sodalite with higher crystallinity but diminished mesoporosity. The collapse of secondary pores and the growth of larger crystals reduce the BET surface area and the number of external catalytic sites, which explains the slight decline in biodiesel yield and catalytic activity.

The composition of the RTO based on the GC-MS analysis is illustrated in Fig. 7. In general, RTO contains palmitic, linoleic, stearic, linolenic, and oleic acids. The highest contents were linoleic (33.21%) and linolenic acids (20.75%). The free fatty acid (FFA) content of the feedstock is one of the important parameters that influences the transesterification reaction. The FFA content in RTO is 2.87%. A low FFA content is required to maximize biodiesel yield during the transesterification reaction, as a high FFA content can cause saponification and soap formation, leading to a decrease in conversion and yield.[40]

Saponification is prevented from occurring during transesterification because it could not only reduce biodiesel yield
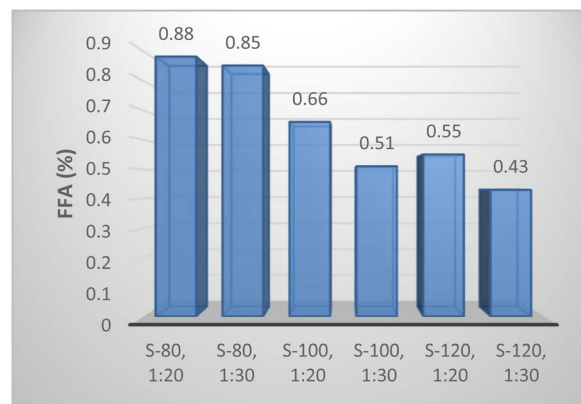

Fig. 8 FFA content of the biodiesel samples with variations in the catalyst and oil-to-methanol ratios.

but also inhibit the separation of esters from glycerol. Consequently, feedstocks with a high FFA content need to be pretreated through an esterification reaction. This reaction is particularly useful for oils or fats with a high FFA content. The FFA content of biodiesel samples produced using various catalysts and oil-to-methanol ratios is depicted in Fig. 8. The optimum FFA content obtained using the S-120 catalyst was 0.43% at a molar ratio of 1 : 30 (oil-to-methanol). The lowest oil-to-biodiesel conversion (63.25%) was achieved using the S-80 catalyst at a molar ratio of 1 : 20 (methanol-to-oil), as shown in Fig. 8.

The highest oil conversion (81.79%) was obtained using the S-100 catalyst at a molar ratio of 1 : 30 (methanol-to-oil). The optimum methyl ester yield achieved using S-100 was 94.14% at a molar ratio of 1 : 30 (oil-to-methanol), as shown in Fig. 10. The high biodiesel yield is attributed to the presence of NaOH on the
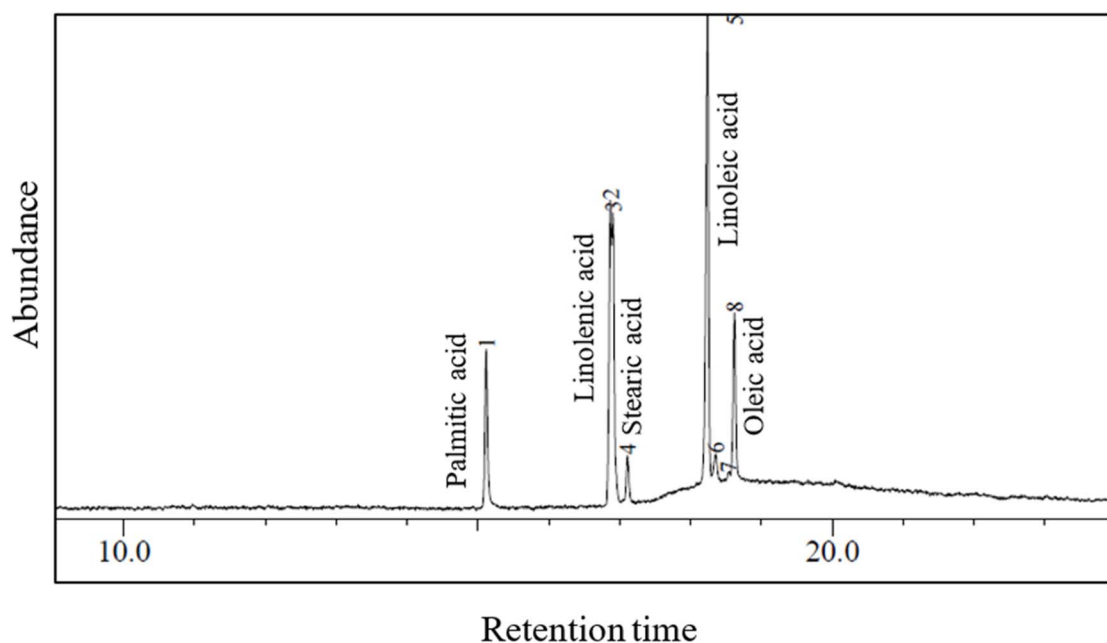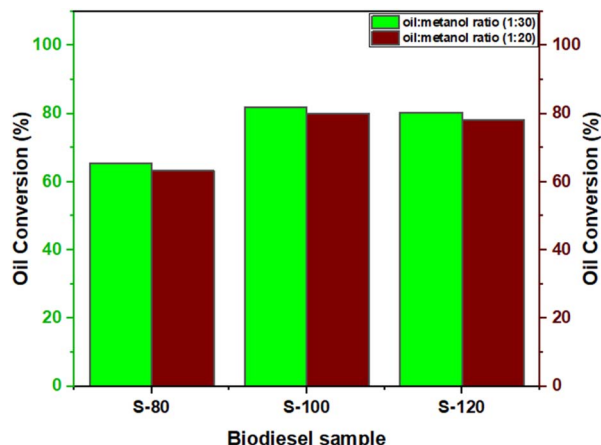

Fig. 7 Chromatogram of RTO.

Fig. 9 Conversion of oil to biodiesel with different catalysts and oil-to-methanol molar ratios.

surface of sodalite during synthesis. However, the yield slightly decreased when the S-120 catalyst was used, reaching 93.44%, despite maintaining the same oil-to-methanol ratio. In principle, a large amount of methanol can contribute to the reaction, which benefits the final product, although it may involve some drawbacks, such as a higher cost. Nevertheless, under heterogeneous conditions, methanol excess can be valuable because glycerol dissolves in methanol, facilitating the removal of by-products from the catalyst surface and supporting catalyst reuse.[41] As displayed in Fig. 9 and 10, the oil-to-methanol molar ratio can significantly influence the reaction outcome, where increasing the ratio from 20 : 1 to 30 : 1 is sufficient to enhance both conversion and biodiesel yield. Additionally, the loss of active sites on sodalite can be attributed to reduced structural stability, as the S-120 catalyst exhibits a lower surface area and mesoporosity. A high concentration of NaOH in the synthesis solution also promotes the formation of Si–O–Na groups within the zeolite structure, which act as active sites during the transesterification process and contribute to the increased biodiesel yield.
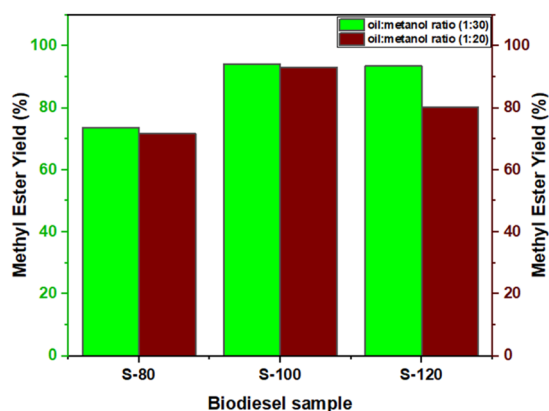

Fig. 10 Methyl ester yield of biodiesel with different catalysts and oil-to-methanol molar ratios.

The superior catalytic performance of S-100 can be directly attributed to its higher mesopore surface area (16.89 m^2 g^{-1}), which provides more accessible active sites for the transesterification reaction. In heterogeneous catalysis, mesopores (2–50 nm) play a crucial role in facilitating the diffusion of bulky triglyceride molecules and methanol into the catalyst framework. The larger mesoporous channels in S-100 reduce mass transfer limitations, allowing the reactants to reach internal active sites more efficiently than in S-80 and S-120. As a result, the reaction kinetics are accelerated, ensuring that triglycerides are more completely converted into methyl esters. This enhanced accessibility explains why S-100 achieved the highest biodiesel yield (94.14%) and conversion (81.79%).

The reuse of the S-100 catalyst was investigated over consecutive reaction cycles under the following conditions: a catalyst loading of 4 wt%, a reaction time of 2 hours, a methanol-to-oil molar ratio of 30 : 1, and a reaction temperature of 65 °C. The results indicated that the methyl ester yields obtained were 94.14%, 90.31%, 84.23%, and 79.68% for the first–fourth cycles, respectively, as illustrated in Fig. 11. The overall reduction in methyl ester yield from the first cycle (94.14%) to the fourth cycle (79.68%) was 14.46%. The gradual decline in catalyst activity with increasing reuse cycles during biodiesel production can be attributed to the fouling of the active sites and the progressive occupation of these sites on the catalyst surface by unreacted triglycerides.[46] This phenomenon resulted in a reduction in both porosity and specific surface area, thereby decreasing the methyl ester yield. Nevertheless, the yield obtained after four consecutive cycles remained relatively high, indicating that the catalyst can be effectively reused for up to four cycles before significant deactivation occurs. Similar findings have been reported by other researchers on the reuse of heterogeneous catalysts for biodiesel production, where a decline in biodiesel yield was observed after multiple cycles.[47–49]

The data in Table 7 show that catalytic performance in biodiesel production generally decreases with successive cycles, indicating catalyst deactivation over time. Canola oil with Mg–Zr/CaO, waste frying oil with MoO$_3$/RHA–CoFe$_2$O$_4$, and *Reutealis trisperma* oil with sodalite (S-100) exhibit relatively high initial yields (>94%) but a gradual decline across four cycles. This reduction can be attributed to several factors, including pore blocking or fouling by glycerol, which physically blocks access to active sites and reduces the surface area and pore volume. In addition, other causes include leaching and the chemical loss of active species in heterogeneous basic catalysts (*e.g.*, CaO and Na-bearing materials). Alkali or alkaline earth ions can dissolve into methanol or water phases, or form carbonates and soaps, leading to the loss of catalytic basic sites. For example, Mg–Zr/CaO decreased from 96.7% to 84% over four cycles, while sodalite-based catalysts decreased from 94.14% to 79.68%, suggesting that alkaline catalysts are prone to leaching in methanol-rich environments, reducing their reusability. Interestingly, palm kernel shell ash exhibited the most stable reusability, maintaining yields above 89% even after the fourth cycle. This could be due to its carbonaceous and mineral composition, which resists leaching and maintains surface

Table 7 Comparison of the biodiesel yields from the reuse of different types of catalysts

Feedstock	Catalyst	First cycle	Second cycle	Third cycle	Fourth cycle	References
		Yield (%)				
Canola oil	7.5% Mg–Zr/CaO	96.7	91.3	88.1	84	Talebi et al.[42]
Used palm cooking oil	Palm kernel shell ash	99.01	94.41	91.70	89.49	Novita et al.[43]
Waste frying oil	30-MoO$_3$/RHA-CoFe$_2$O$_4$	94.6	94.5	91.1	89.1	Gonçalves et al.[44]
Used palm cooking oil	Phosphate mesoporous zirconia impregnated with calcium oxide	86.49	83.02	78.37	63.33	Sambara et al.[45]
Reutealis trisperma oil	S-100 (sodalite)	94.14	90.31	84.23	79.68	This work

basicity. In contrast, phosphate mesoporous zirconia impregnated with CaO showed the fastest deactivation, with the yield decreasing from 86.49% to just 63.33%, likely due to significant CaO leaching and pore blockage. These comparisons highlight that while high biodiesel yields can be achieved in the first cycle with various catalysts, long-term stability is highly dependent on catalyst structure, resistance to leaching, and the ability to withstand carbon deposition or poisoning during repeated use.

Catalyst regeneration in biodiesel production is a crucial step in restoring activity after multiple reaction cycles, as heterogeneous catalysts are prone to fouling, leaching, and surface poisoning. Two of the most common regeneration strategies are washing and calcination, each of which addresses different deactivation mechanisms. The washing-based regeneration method involves cleaning the spent catalyst using solvents (e.g., methanol, ethanol, hexane, or acetone) to remove adsorbed organic residues, such as unreacted triglycerides, glycerol, free fatty acids, and soaps. These residues typically block the pores and cover the active sites, reducing catalytic efficiency. Solvent washing dissolves these organic deposits, while acid washing (using dilute HCl or acetic acid) is sometimes employed to remove carbonate deposits or neutralize surface soaps.[50] This method is relatively mild and preserves the catalyst's structure, making it suitable for catalysts with limited thermal stability, such as zeolites. However, calcination-based regeneration relies on thermal treatment in air at elevated temperatures (typically 400–600 °C, depending on the catalyst material). This process decomposes and burns off

carbonaceous deposits (coke), polymerized glycerol, and residual hydrocarbons, leaving behind a cleaner surface and reopening blocked pores. Calcination is particularly effective for solid base catalysts; however, excessive heating may cause sintering, phase transformation, or collapse of porous structures, thereby reducing surface area and limiting reusability.[51]

The FTIR spectra of biodiesel created from RTO are depicted in Fig. 12. The absorption band at 3484 cm^{-1} was associated with the O–H bond stretching vibration, while the sharp peaks at 2933 cm^{-1} and 2853 cm^{-1} were linked to the asymmetric and
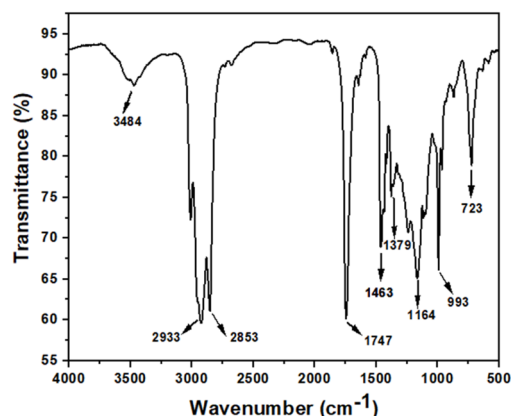

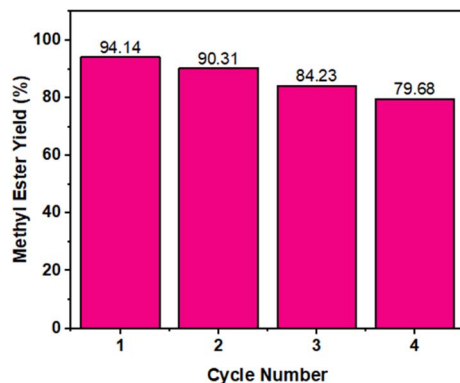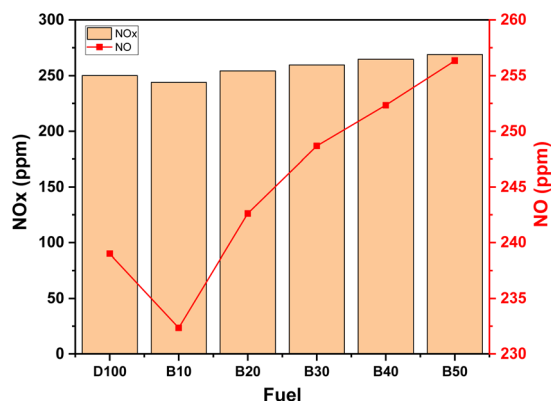**Fig. 12** IR spectra of the biodiesel sample using the S-100 catalyst.

Fig. 11 Reuse of the S-100 catalyst.

Fig. 13 Comparison of the NO and NO$_x$ emissions from various biodiesel–diesel fuel blends.

symmetric vibrations of CH bonds in CH_2 and CH_3 groups, respectively. The band at 1747 cm^{-1} corresponded to the C=O stretching vibration of the triglyceride carbonyl group.[52] Absorptions in the 1500–1200 cm^{-1} range were attributed to the bending vibrations of aliphatic CH_2 and CH_3 groups. Peaks at 1463 cm^{-1} and 1379 cm^{-1} represented the bending vibrations of HCH and CH_2. The absorption at 1164 cm^{-1} was due to the stretching vibration of the C–O ester. The peak at 723 cm^{-1} indicated overlapping vibrations of $(CH_2)_n$.[53] The stretching vibrations of CH, CH_2, and CH_3 were evident in the 2700–3500 cm^{-1} range, while their bending vibrations were observed in the range of 700–1500 cm^{-1}.[54]

Fig. 13 illustrates the NO and NO_x emission results for each tested fuel blend. The highest NO emission was observed for the B50 blend (256.34 ppm), whereas the lowest was recorded for B10 (232.34 ppm). Similarly, the NO_x emission reached a maximum of 268.67 ppm for B50 and a minimum of 243.92 ppm for B10. The NO and NO_x emission levels are influenced by the oxygen content in the combustion chamber and are associated with elevated combustion temperatures. As the oxygen concentration increases, NO_x emissions tend to rise accordingly.[55,56] The concentrations of NO and NOx emissions were found to increase with higher biodiesel blending ratios compared to pure diesel fuel.[57,58]

The carbon monoxide (CO) emission results for biodiesel–diesel fuel blends are presented in Fig. 14. The highest CO emission (278.67 ppm) was recorded for pure diesel (D100), whereas the lowest (170.44 ppm) was observed for B50. The maximum CO emission reduction efficiency achieved was 38.84%. An increase in the biodiesel blending ratio led to a significant reduction in CO emissions. The formation of CO during combustion is an exothermic process, commonly referred to as catalytic oxidation. Carbon monoxide is produced when there is insufficient oxygen during combustion, resulting in incomplete oxidation of carbon atoms to carbon dioxide.[59] CO emissions depend on oxygen availability, carbon content, and combustion efficiency. During combustion, the carbon in the fuel is oxidized, converting CO to CO_2. A lack of oxygen leads to incomplete combustion, producing higher CO emissions.[55,60] Similar findings were reported by Fareed *et al.*, who observed a consistent trend in their emission studies, where increasing biodiesel blend ratios resulted in lower CO emission levels.[61]

Conclusions

This study presents the utilization of RTO for biodiesel production using a sodalite nanocatalyst synthesized from natural kaolin. XRD and FTIR characterization results indicated that a pure sodalite phase began to form at a crystallization temperature of 100 °C. SEM–EDX analysis revealed that the synthesized catalyst exhibited agglomerated spherical morphologies with a particle size of approximately 20 nm. The transesterification results showed that the sodalite catalyst achieved an RTO conversion of up to 81.79%, with an optimum methyl ester yield of 94.14% using the S-100 catalyst. The Si–O–Na functional groups acted as active sites within the sodalite framework, thereby enhancing biodiesel yield. Nevertheless, the catalyst exhibited a gradual decline in activity after four consecutive cycles, indicating fouling and deactivation of the active sites. This limitation highlights the need for regeneration strategies, such as washing or calcination, to maintain the catalyst's long-term performance. Emission tests revealed that biodiesel blends produced lower CO emissions compared to pure diesel fuel, whereas NO and NOx emissions tended to increase with higher biodiesel blend ratios. This study is the first to report the direct conversion of Indonesian natural kaolin into sodalite for biodiesel catalysis. Future work will focus on scaling up the process, performing life-cycle and techno-economic analyses, testing the catalyst on a wider range of non-edible oils, and developing strategies to further improve catalyst stability and reusability.

Author contributions

Abdul Hamid: conceptualization, investigation, validation, formal analysis, data curation, writing – original draft; Yusuf Widayanto: methodology, data curation, formal analysis and visualization; Zeni Rahmawati: validation, supervision, funding acquisition, writing – review & editing; Misbakhul Fatah: supervision, conceptualization, and validation; Tri Esti Purbaningtyas: formal analysis, data analysis and visualization; Tri Wahyuni: validation, writing – review & editing; and Ike Dayi Febriana: data analysis and formal analysis.

Conflicts of interest

The authors declare that they have no known competing financial interests or personal relationships that could have appeared to influence the work reported in this paper.

Data availability

The authors confirm that the data supporting the findings of this study are available within the article. No primary research results, software or code has been included and no new data were generated or analysed as part of this review.
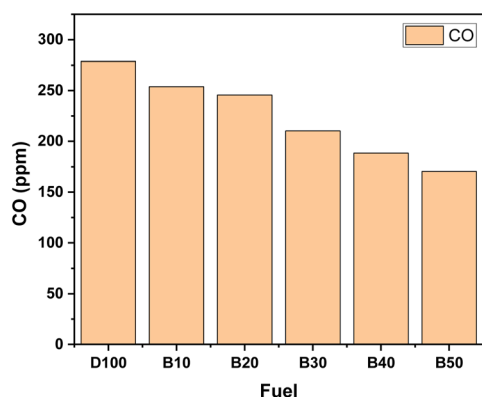

Fig. 14 Comparison of the CO emissions from various biodiesel–diesel fuel blends.

Acknowledgements

Notes and references

1 R. Shalihah, N. Widiarti, E. Yanuar and D. Prasetyoko, *Malays. J. Fundam. Appl. Sci.*, 2020, **16**, 649–653.

2 M. T. Darwin, M. Alwi, Z. Murizal, A. Pratama and M. Rizal, *Case Stud. Chem. Environ. Eng.*, 2023, **8**, 100512.

3 M. Iuliano, M. Sarno, S. De Pasquale and E. Ponticorvo, *Renewable Energy*, 2020, **162**, 124–133.

4 M. R. Abukhadra, M. Mostafa, A. M. El-Sherbeeny, A. T. Ahmed Soliman and A. E. E. Abd Elgawad, *Microporous Mesoporous Mater.*, 2020, **306**, 110465.

5 L. Wu, T. Y. Wei, Z. F. Tong, Y. Zou, Z. J. Lin and J. H. Sun, *Fuel Process. Technol.*, 2016, **144**, 334–340.

6 S. Nurjanah, D. S. Lestari, A. Widyasanti and S. Zain, *Int. J. Adv. Sci. Eng. Inf. Technol.*, 2015, **5**, 52–56.

7 H. Holilah, D. Prasetyoko, T. P. Oetami, E. B. Santosa, Y. M. Zein, H. Bahruji, H. Fansuri, R. Ediati and J. Juwari, *Biomass Convers. Biorefin.*, 2015, **5**, 347–353.

8 Z. Rahmawati, H. Holilah, S. W. Purnami, H. Bahruji, T. P. Oetami and D. Prasetyoko, *Bull. Chem. React. Eng. Catal.*, 2021, **16**, 686–695.

9 S. Maroa and F. Inambao, *Eng. Life Sci.*, 2021, **21**, 790–824.

10 N. Anil, P. K. Rao, A. Sarkar, J. Kubavat, S. Vadivel, N. R. Manwar and B. Paul, *Energy Convers. Manage.*, 2024, **318**, 118884.

11 S. M. Farouk, A. M. Tayeb, S. M. S. Abdel-Hamid and R. M. Osman, *Environ. Sci. Pollut. Res.*, 2024, **31**, 12722–12747.

12 M. Sharifi, S. Tangestaninejad, M. Moghadam, A. Marandi, V. Mirkhani, I. Mohammadpoor-Baltork and S. Aghayani, *Sci. Rep.*, 2025, **15**, 3610.

13 G. Yang and J. Yu, *Chemistry*, 2023, **5**, 438–451.

14 A. Hamid, R. E. Nugraha, H. Holilah, H. Bahruji and D. Prasetyoko, *J. Korean Ceram. Soc.*, 2022, 1–13.

15 E. Olusola Oke, K. Kolapo Salam, T. Deborah Oluwole, A. Eze Okere, N. Darlington, K. Ayoola Babatunde, Y. Umar and S. Omolara Ibrahim, *Cleaner Mater.*, 2024, **11**, 100233.

16 S. Supriyadi, P. Purwanto, D. D. Anggoro and H. Hermawan, *Automotive Experiences*, 2022, vol. 5, pp. 57–67.

17 R. Shalihah, N. Widiarti, E. Yanuar and D. Prasetyoko, *Malays. J. Fundam. Appl. Sci.*, 2020, **16**, 649–653.

18 T. M. I. Riayatsyah, R. Thaib, A. S. Silitonga, J. Milano, A. H. Shamsuddin, A. H. Sebayang and J. Sutrisno, *Sustainability*, 2021, **13**, 1–15.

19 Z. Rahmawati, H. Holilah, S. W. Purnami, H. Bahruji, T. P. Oetami and D. Prasetyoko, *Bull. Chem. React. Eng. Catal.*, 2021, **16**, 686–695.

20 K. Kusmiyati, D. Prasetyoko, S. Murwani, M. N. Fadhilah, T. P. Oetami, H. Hadiyanto, W. Widayat, A. Budiman and A. Roesyadi, *Energies*, 2019, **12**, 3714.

21 T. R. F. Suprapto, M. S. Sangi, T. P. Oetami, I. Qoniah and D. Prasetyoko, *Indones. J. Chem.*, 2016, **16**, 208–213.

22 L. Suriyanti, T. Usman and W. Rahmalia, *Indones. J. Chem.*, 2024, **24**, 691–700.

23 A. Selemani and G. G. Kombe, *Results Eng.*, 2022, **16**, 100602.

24 C. Pansakdanon, P. Seejandee, S. Kosawatthanakun, K. Deekamwong, S. Prayoonpokarach and J. Wittayakun, *J. Phys. Chem. Solids*, 2025, **196**, 112389.

25 N. Widiarti, H. Bahruji, H. Holilah, Y. L. Ni'mah, R. Ediati, E. Santoso, A. A. Jalil, A. Hamid and D. Prasetyoko, *Biomass Convers. Biorefin.*, 2023, **13**, 3001–3015.

26 M. Yu, D. Luo, J. Kuang and W. Yuan, *Results Phys.*, 2022, **41**, 105887.

27 J. Vogrin, T. Santini, H. Peng, L. Zhao and J. Vaughan, *Appl. Clay Sci.*, 2023, **244**, 107106.

28 P. Pasabeyoglu, G. Moumin, L. de Oliveira, M. Roeb and B. Akata, *J. Cleaner Prod.*, 2023, **414**, 137611.

29 A. Hamid, R. E. Nugraha, H. Holilah, H. Bahruji and D. Prasetyoko, *J. Korean Ceram. Soc.*, 2023, **60**, 344–356.

30 L. Cui, R. Han, L. Yang, Y. Wu, R. Pei and F. Li, *Microporous Mesoporous Mater.*, 2020, **306**, 110385.

31 D. Arepalli, A. ur Rehman, M. Z. Kim, S. F. Alam and C. H. Cho, *Microporous Mesoporous Mater.*, 2022, **329**, 111451.

32 A. Táborosi, R. K. Szilagyi, B. Zsirka, O. Fónagy, E. Horváth and J. Kristóf, *Inorg. Chem.*, 2018, **57**, 7151–7167.

33 H. Xu, X. Jin, P. Chen, G. Shao, H. Wang, D. Chen, H. Lu and R. Zhang, *Ceram. Int.*, 2015, **41**, 6463–6469.

34 S. Salimkhani, K. Siahcheshm, A. Kadkhodaie and H. Salimkhani, *Mater. Chem. Phys.*, 2021, **271**, 124957.

35 N. A. Sholeha, L. Jannah, H. N. Rohma, N. Widiastuti, D. Prasetyoko, A. A. Jalil and H. Bahruji, *Clays Clay Miner.*, 2020, **68**, 513–523.

36 M. Ulfa, A. Masykur, A. F. Nofitasari, N. A. Sholeha, S. Suprapto, H. Bahruji and D. Prasetyoko, *Materials*, 2022, **15**, 2745.

37 Q. Song, J. Shen, Y. Yang, J. Wang, Y. Yang, J. Sun, B. Jiang and Z. Liao, *Microporous Mesoporous Mater.*, 2020, **292**, 109755.

38 J. Jiang, X. Gu, L. Feng, C. Duanmu, Y. Jin, T. Hu and J. Wu, *Powder Technol.*, 2012, **217**, 298–303.

39 R. E. Nugraha, D. Prasetyoko, N. A. Nareswari, A. Aziz, H. Holilah, H. Bahruji, M. R. Yusop, N. Asikin-Mijan, S. Suprapto, Y. H. Taufiq-Yap, A. A. Jalil, S. W. Purnami and H. Hartati, *Case Stud. Chem. Environ. Eng.*, 2024, **10**, 100877.

40 M. E. Di Pietro, A. Mannu and A. Mele, *Processes*, 2020, **8**, 410.

41 A. Aloia, M. Izzi, A. Rizzuti, M. Casiello, P. Mastrorilli, N. Cioffi, A. Nacci, R. A. Picca and A. Monopoli, *Mol. Catal.*, 2024, **560**, 114128.

42 M. Talebi, A. Larimi, F. Khorasheh and T. N. Borhani, *Sustainable Chem. Pharm.*, 2024, **39**, 101559.

43 L. Novita, E. Safni, F. A. de Freitas, S. Fauzia and R. Zein, *Case Stud. Chem. Environ. Eng.*, 2024, **9**, 100678.

44 M. A. Gonçalves, H. C. L. dos Santos, T. S. Ribeiro, A. da Cas Viegas, G. N. da Rocha Filho and L. R. Vieira da Conceição, *RSC Adv.*, 2024, **14**(29), 20743–20756.

45 E. C. Sambara, A. J. Saviola, A. Syoufian, R. A. Fitria, A. Mumtaziyah, K. Rozana, W. C. Oh, B. Ravindran, W. D. Saputri, A. K. Amin, D. A. Saputra, S. Rahayu and K. Wijaya, *Next Mater.*, 2025, **9**, 101147.

46 M. Talebi, A. Larimi, F. Khorasheh and T. N. Borhani, *Sustainable Chem. Pharm.*, 2024, **39**, 101559.

47 B. Oladipo, S. Qasana, S. C. Zini, N. Menemene and T. V. Ojumu, *Fuel Process. Technol.*, 2024, **266**, 108161.

48 E. Betiku, K. E. Okpalaeke, B. A. Sotunde and T. V. Ojumu, *Biomass Bioenergy*, 2025, **193**, 107525.

49 O. Kanwal, R. Emmanuel, U. Micheal and M. Zafar, *Waste Manag. Bull.*, 2025, **3**, 27–38.

50 V. Makarevičienė, I. Gaidė and E. Sendžikienė, *Catalysts*, 2025, **15**, 957.

51 I. de Araújo Sobrinho, T. S. Ribeiro, A. C. Dias e Silva, M. Arrais Gonçalves, G. N. da Rocha Filho and L. R. Vieira da Conceição, *RSC Adv.*, 2025, **15**, 7050–7068.

52 J. Nisar, R. Razaq, M. Farooq, M. Iqbal, R. A. Khan, M. Sayed, A. Shah and I. ur Rahman, *Renewable Energy*, 2017, **101**, 111–119.

53 E. A. Shalaby and N. Sh El-Gendy, Two steps alkaline transesterification of waste cooking oil and quality assessment of produced biodiesel, *Int. J. Chem. Biochem. Sci.*, 2012, **1**, 30–35.

54 M. Tariq, S. Ali, F. Ahmad, M. Ahmad, M. Zafar, N. Khalid and M. A. Khan, *Fuel Process. Technol.*, 2011, **92**, 336–341.

55 N. G. Mengistu, M. W. Mekonen, Y. G. Ayalew, L. F. Demisie and T. Nega, *Discover Energy*, 2024, **4**, 26.

56 R. Singh, G. Pradhan, S. Pradhan and D. Madhu, *Waste Biomass Valorization*, 2024, **15**, 2133–2144.

57 M. Jamshaid, H. H. Masjuki, M. A. Kalam, N. W. M. Zulkifli, A. Arslan and A. A. Qureshi, *Energy*, 2022, **239**, 121894.

58 S. I. S. Mohammad, A. Vasudevan, K. D. V. Prasad, I. R. Ali, A. Kumar, A. Kulshreshta, V. S. Mann, I. B. Sapaev, T. Kalyani and M. Sina, *Heliyon*, 2025, **11**, 41416.

59 A. Hamid, A. Jakfar, S. B. Romaniyah, I. D. Febriana, M. Abdullah, Z. Rahmawati and D. Prasetyoko, *Automotive Experiences*, 2023, **6**, 80–93.

60 J. Jayaprabakar, S. S. Dawn, M. Anish, J. Giri, K. Sudhakar, A. A. Alarfaj and A. Guru, *Heliyon*, 2024, **10**, 37118.

61 A. F. Fareed, A. S. El-Shafay, M. A. Mujtaba, F. Riaz and M. S. Gad, *Case Stud. Therm. Eng.*, 2024, **60**, 104721.